Dissipative particle dynamics simulation of depletion layer and polymer migration in micro- and nanochannels for dilute polymer solutions

Dmitry A. Fedosov,[1] George Em Karniadakis,[1,a)] and Bruce Caswell[2]

[1]*Division of Applied Mathematics, Brown University, Providence, Rhode Island 02912, USA*
[2]*Division of Engineering, Brown University, Providence, Rhode Island 02912, USA*

The flows of dilute polymer solutions in micro- and nanoscale channels are of both fundamental and practical importance in variety of applications in which the channel gap is of the same order as the size of the suspended particles or macromolecules. In such systems depletion layers are observed near solid-fluid interfaces, even in equilibrium, and the imposition of flow results in further cross-stream migration of the particles. In this work we employ dissipative particle dynamics to study depletion and migration in dilute polymer solutions in channels several times larger than the radius of gyration (R_g) of bead-spring chains. We compare depletion layers for different chain models and levels of chain representation, solvent quality, and relative wall-solvent-polymer interactions. By suitable scaling the simulated depletion layers compare well with the asymptotic lattice theory solution of depletion near a repulsive wall. In Poiseuille flow, polymer migration across the streamlines increases with the Peclet and the Reynolds number until the center-of-mass distribution develops two symmetric off-center peaks which identify the preferred chain positions across the channel. These appear to be governed by the balance of wall-chain repulsive interactions and an off-center driving force of the type known as the Segre–Silberberg effect. © *2008 American Institute of Physics*. [DOI: 10.1063/1.2897761]

I. INTRODUCTION

Polymer depletion and cross-stream migration phenomena in micro- and nanochannels are important in microfluidic devices and a variety of biological systems. These effects might be relevant in physical processes such as adsorption, lubrication, wall slip, and polymer transport. Depletion layers arise from steric wall repulsion,[1,2] when a polymer solution is placed in confined geometries. Depletion was observed in the region next to the fluid-solid interface in several experiments,[3,4] and was simulated using various methods including Monte Carlo (MC),[5–7] lattice Boltzmann (LBM),[8,9] Brownian dynamics (BD),[9,10] and dissipative particle dynamics (DPD).[11] An asymptotic analytical solution[12] of the depletion layer for an ideal chain in the presence of purely repulsive wall predicts depletion to be effective at about of one radius of gyration from the confining surface. Therefore, in micro- and nanochannels the layer is often of the same order as the channel width, and greatly affects the polymer distribution across the channel.

In presence of flow (e.g., Poiseuille, Couette) the polymer migration phenomena changes the polymer distribution across the channel. Several experimental observations[3,4] show polymer migration from the walls towards the channel centerline. However, simulations[8,10,11,13] showed that polymer migration might proceed towards the walls as well as to the channel centerline. Two models of polymer migration which emphasize the importance of polymer hydrodynamic interactions were recently proposed by Graham *et al.*[14] and

by Ladd *et al.*[13] The former predicts polymer migration away from the walls and attributes this effect to wall-polymer hydrodynamic interactions and a gradient in chain mobility. The latter states that polymer migration can proceed both away from and to the wall, and is determined by the balance of several effects: hydrodynamic lift, rotation, and drift of the polymer. Recent simulations[8–11] of polymer migration in Poiseuille flow showed a development of two symmetric off-center peaks (local maxima) in the polymer distribution between the wall and the centerline. These peaks become more pronounced with increasing Peclet or Reynolds number. In contrast, the polymer distribution in Couette flow yielded a single local maximum at the channel centerline. Thus, the presence of two symmetric off-center peaks in pressure-driven Poiseuille flow appears to be related to variable shear rates. The above unresolved issues suggest further investigation.

Here we employ dissipative particle dynamics[15,16] to investigate the depletion layer and polymer migration. DPD is a mesoscopic method that can potentially bridge the gap between the atomistic and the continuum descriptions of fluids. The DPD particles represent *clusters* of molecules moving together in a Lagrangian fashion subject to soft quadratic potentials. In contrast to molecular dynamics method, DPD employs much larger time steps and particle sizes due to soft particle interactions. In particular, the DPD method appears to be successful in simulations of complex fluids, such as suspensions of polymers, DNA, and colloids in a Newtonian incompressible solvent, etc., see Refs. 17–19. In this paper, we systematically investigate the dependence of wall-polymer depletion on the polymer model, level of chain rep-

a)Author to whom correspondence should be addressed. Electronic mail: gk@dam.brown.edu.
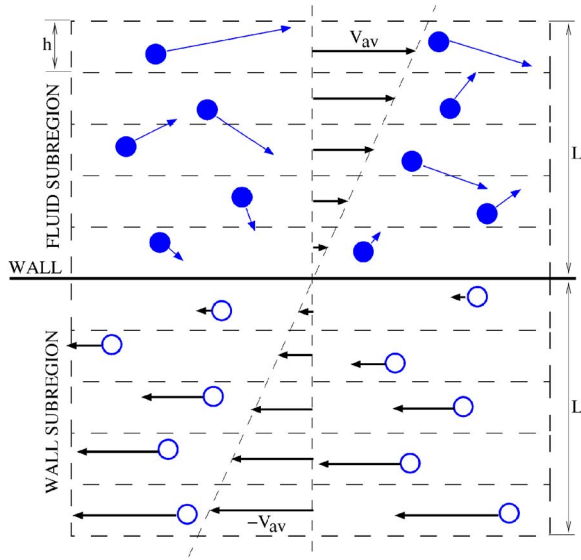
FIG. 1. (Color online) The equilibrium boundary condition with shear procedure (EBC-S).

resentation, solvent quality, and relative wall-polymer-solvent interactions. By means of suitable scaling of simulated depletion layers we compare our results to the asymptotic lattice theory solution[12] of depletion near a repulsive wall. Also, we investigate polymer migration in Poiseuille flow, and we offer an argument which attributes polymer migration to wall-polymer hydrodynamic interactions and to the well-known Segre–Silberberg effect.[20,21]

The paper is organized as follows. In the next section we present some details of the DPD governing equations, the polymer models, and the boundary conditions. In Sec. III we present simulation results for a polymer solution in a channel in the static case (no net flow). In Sec. IV we present migration results for dilute-solution Poiseuille flow at different Peclet and Reynolds numbers. We conclude in Sec. V with a brief discussion.

II. DPD MODEL

A. DPD governing equations

DPD is a mesoscopic particle method, where each particle represents a *molecular cluster* rather than an individual atom, and can be thought of as a soft lump of fluid. The DPD system consists of N point particles of mass m_i, position $\mathbf{r}_i$, and velocity $\mathbf{v}_i$. DPD particles interact through simple pairwise-additive forces corresponding to a conservative force $\mathbf{F}_{ij}^C$, a dissipative force $\mathbf{F}_{ij}^D$, and a random force $\mathbf{F}_{ij}^R$. The total force exerted on a particle i by particle j consists of the three terms given by

$$\mathbf{F}_{ij}^C = F_{ij}^C(r_{ij})\hat{\mathbf{r}}_{ij}, \tag{1}$$

$$\mathbf{F}_{ij}^D = -\gamma\omega^D(r_{ij})(\mathbf{v}_{ij}\cdot\hat{\mathbf{r}}_{ij})\hat{\mathbf{r}}_{ij}, \tag{2}$$

$$\mathbf{F}_{ij}^R = \sigma\omega^R(r_{ij})\xi_{ij}\hat{\mathbf{r}}_{ij}, \tag{3}$$

where $\mathbf{r}_{ij}=\mathbf{r}_i-\mathbf{r}_j$, $r_{ij}=|\mathbf{r}_{ij}|$, $\hat{\mathbf{r}}_{ij}=\mathbf{r}_{ij}/r_{ij}$, and $\mathbf{v}_{ij}=\mathbf{v}_i-\mathbf{v}_j$. The coefficients γ and σ determine the strength of dissipative and random forces, respectively. ω^D and ω^R are weight functions,

TABLE I. DPD simulation parameters.

n	r_c	γ	σ	k_BT
3	1	4.5	3	1

ξ_{ij} is a normally distributed random variable with zero mean, unit variance, and $\xi_{ij}=\xi_{ji}$. All forces act within a sphere of radius r_c, the *cutoff radius*, which defines the length scale in the DPD system. The conservative force $F_{ij}^C(r_{ij})$ is typically given by

$$F_{ij}^C(r_{ij}) = \begin{cases} a_{ij}(1-r_{ij}/r_c), & \text{for } r_{ij} \leq r_c \\ 0, & \text{for } r_{ij} > r_c, \end{cases} \tag{4}$$

where $a_{ij}=\sqrt{a_i a_j}$ and a_i, a_j are conservative force coefficients for particles i and j, respectively.

The random and dissipative forces must satisfy the fluctuation-dissipation theorem[22] in order for the DPD system to maintain equilibrium temperature T.

$$\omega^D(r_{ij}) = [\omega^R(r_{ij})]^2 \tag{5}$$

$$\sigma^2 = 2\gamma k_BT, \tag{6}$$

where k_B is the Boltzmann constant. The usual choice for the weight functions is

$$\omega^R(r_{ij}) = \begin{cases} (1-r_{ij}/r_c)^p, & \text{for } r_{ij} \leq r_c \\ 0, & \text{for } r_{ij} > r_c, \end{cases} \tag{7}$$

where $p=1$ for the original DPD method. However, other choices (e.g., $p=0.25$) for these envelopes have been used[23–25] in order to increase the viscosity of the DPD fluid and bring the Schmidt number in DPD to values representative of real liquids. The p values used in simulations will be designated below.

The time evolution of velocities and positions of particles is determined by the Newton's second law of motion,

$$d\mathbf{r}_i = \mathbf{v}_i dt, \tag{8}$$

$$d\mathbf{v}_i = \frac{1}{m_i}\sum_{j\neq i}(\mathbf{F}_{ij}^C dt + \mathbf{F}_{ij}^D dt + \mathbf{F}_{ij}^R\sqrt{dt}). \tag{9}$$

The above equations of motion were integrated using the modified velocity-Verlet algorithm.[16]

B. Polymer models

The polymer model in our simulations is based on the well-known linear bead-spring polymer chain representation. Each bead in a polymer chain is subject to three DPD forces mentioned in the previous section and intra-polymer forces arising from neighboring bead-to-bead interactions. Here we consider flexible chains, so two consecutive segments of a chain have no preferred angle between them. Below we outline two spring laws which define force contributions of bead-to-bead interactions.

TABLE II. Simulation parameter sets for different bead-spring models.

spring	k	r_{max}	r_{eq}	a_{ss}	a_{pp}	a_{ps}	a_{wp}	R_g
FENE	10	2	N/A	25	25	17.5	17.5	1.6264
FENE	20	2.5	N/A	25	25	17.5	17.5	1.4437
Fraenkel	10	N/A	0.7	25	25	17.5	17.5	1.9207

1. FENE spring

Each pair of particles connected by the finitely extensible nonlinear elastic (FENE) spring is subject to the nonlinear potential.

$$U_{\text{FENE}} = -\frac{k}{2} r_{max}^2 \log \left[1 - \frac{|\mathbf{r}_i - \mathbf{r}_j|^2}{\mathbf{r}_{max}^2} \right], \qquad (10)$$

where r_{max} is the maximum spring extension and k is the spring constant. When the distance between two connected beads approaches r_{max}, the spring attractive force goes to infinity, and therefore the length greater than r_{max} is not allowed.

2. Fraenkel spring

Two connected beads interact through the quadratic potential with a fixed equilibrium length r_{eq}.

$$U_{\text{Fraenkel}} = \frac{k}{2}(|\mathbf{r}_i - \mathbf{r}_j| - r_{eq})^2, \qquad (11)$$

where k is the spring constant. In contrast to the FENE model, this type of spring virtually has no limit on the maximum allowed distance between two beads. However, the minimum of potential energy corresponds to the length r_{eq} which is preferred equilibrium interbead distance. Sometimes this model is also called the *harmonic* spring.

C. Wall boundary conditions

In order to enforce no-slip boundary condition (BC) at the fluid-solid interface we employ the equilibrium BC model with adaptive shear correction (EBC-S).[25] At the preprocessing stage, the computational domain covers both fluid and solid wall regions and is assumed to be periodic in all directions. The hydrostatic simulation is run until the equi-

librium state is reached. In the solid region the particles are then frozen at some instant of time, and later are used to model solid walls in combination with bounce-back reflection at the fluid-solid interface. In addition, we use an adaptive shear procedure illustrated in the Fig. 1. Subregions of the computational domain of width $L = r_c$ adjacent to the fluid-solid interface in both fluid and wall regions are considered. We divide the fluid and wall subregions into bins of height h, whose value determines the accuracy of the near-wall velocity profile. If the velocity profile changes in the direction parallel to the wall these subregions can be divided into bins along the wall. During the simulation, in each bin in the fluid subregion the time-averaged velocity $\mathbf{v}_{av}$ is collected over a specified number of time steps. The velocities of the particles inside each bin in the wall subregion are set to be opposite, i.e., $-\mathbf{v}_{av}$, to the average velocity in the corresponding fluid subregion bin, which is symmetric with respect to the fluid-solid interface. The wall particles (shown as open circles) do not move in the simulations, and carry only the velocity information needed for the calculation of the dissipative force. A complete description of the BC model can be found in Ref. 25.

III. HYDROSTATICS OF CONFINED DILUTE POLYMER SOLUTIONS

In this section we present results of DPD simulations for the static case of dilute polymer solutions confined between parallel plates separated by gap H. Dilute solutions are composed as a single polymer chain immersed in a Newtonian-type fluid solvent. Numerical measurements are taken of the polymer center-of-mass distribution, the bead distribution, and the stresses across the channel.
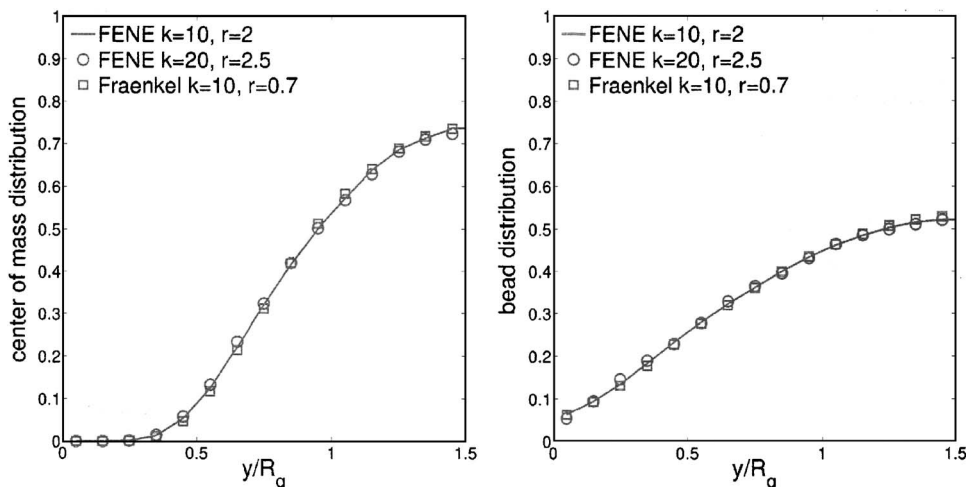

FIG. 2. Center-of-mass (left) and bead (right) distributions for three $N=16$ bead chains.

TABLE III. DPD parameter sets for solvent quality calculations.

spring	solvent	k	r_{max}	r_{eq}	a_{ss}	a_{pp}	a_{ps}	a_{wp}	R_g
FENE	good	20	2	N/A	25	25	17.5	17.5	4.7373
FENE	poor	20	2	N/A	25	25	25	25	3.9235
Fraenkel	ideal	10	N/A	0.7	0	0	0	0	3.5691

A. Simulation parameters

Table I presents the parameters used in DPD simulations. The number density n of a solution includes solvent and polymer particles. The conservative force coefficients will be specified in text corresponding to a particular simulation. All simulations employed the modified velocity-Verlet integration scheme with $\lambda = 0.5$[16], which corresponds to the standard velocity-Verlet scheme widely used in molecular dynamics simulations. The time step was set to 0.01. Solid walls were placed at $y=0$ and $y=H$, and modeled by freezing DPD particles at equilibrium in combination with bounce-back reflection at the fluid-solid interface. The number density of the walls was that of fluid. In addition, adaptive shear procedure (EBC-S type[25]) was used in order to enhance dissipative interactions and ensure no-slip condition at the fluid-solid interface. For EBC-S we used a $1 \times 5 \times 1$ bin grid for all walls in order to compute the near-wall velocity profile and mimic a counter flow in the wall region.

B. Simulations with several bead-spring models

Employing two different spring models we performed several DPD simulations of a chain in a static solvent in the channel described above. The polymer chain consists of 16 beads. Three sets of simulation parameters are shown in Table II, where a_{ss} is the repulsive force coefficient between solvent-solvent particles, a_{pp}—polymer-polymer (beads), a_{ps}—polymer-solvent, and a_{wp}—wall-polymer particles, respectively. R_g is the polymer radius of gyration obtained from equilibrium simulations of dilute solution in large enough periodic domain. The choice of repulsive interactions defines a polymer solution with good quality solvent, which was pointed out in Ref. 26. The exponent p in Eq. (7) was set to 0.25 that corresponds to the kinematic viscosity of a fluid 0.54, which was obtained using the periodic Poiseuille flow

method of Ref. 27. The height of the channel H was set to $3R_g$. In the other two dimensions, system is periodic and has a length more than $2H$ in order to ensure no dependence of the results from the domain size. The simulation times were set to allow the chain diffusion distance to be at least $40H$. Furthermore, 32 statistically independent copies (trajectories) of each simulation were run simultaneously on a Blue Gene supercomputer. The combination of trajectories and long enough run times provided us with smooth chain center-of-mass results even though only one polymer chain is present in the simulation domain.

The results revealed that the polymer center-of-mass and the bead distributions across the channel collapse onto one curve for all three simulations. Figure 2 shows the center-of-mass distribution (left) and polymer bead distribution (right) for three polymer chains with the distance from the wall normalized by R_g. These and all subsequent distributions are shown over the half channel because of symmetry with respect to the centerline, and hence they have been normalized with area of one half. Thus, it appears that polymer distribution in dilute solution is independent of polymer model used, and is correlated only by a mesoscopic polymer characteristic length such as the radius of gyration or the end-to-end distance.

C. Effect of the solvent quality

Polymers and macromolecules can have dissimilar properties and behavior in different solvents. In fact, polymer characteristics can drastically change depending on the solvent quality. It is well known that the quality of the solvent exhibits different scaling laws for static and dynamic polymer properties (e.g., R_g, D). Here, we performed DPD simulations to identify the effect of solvent quality on the polymer distribution in the channel. We compare ideal chains to
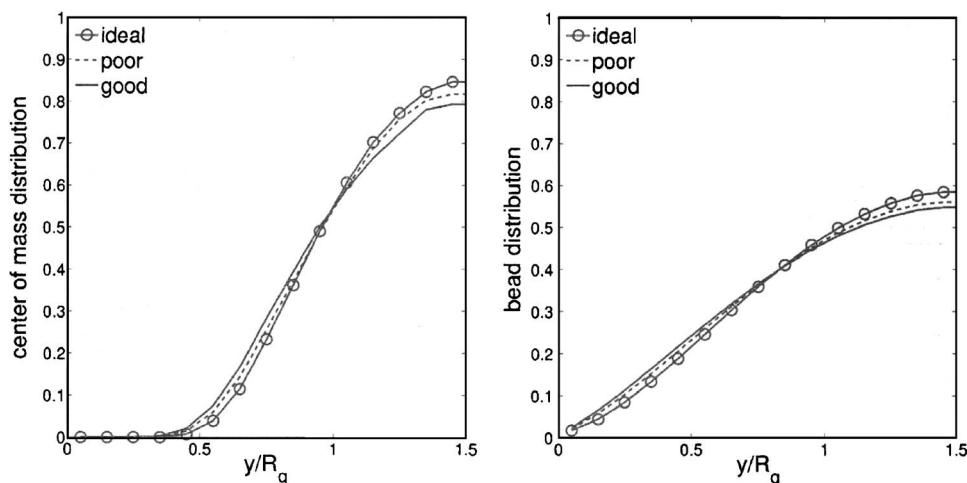

FIG. 3. Effect of the solvent quality on the center-of-mass (left) and bead (right) distributions for $N=100$ chains.
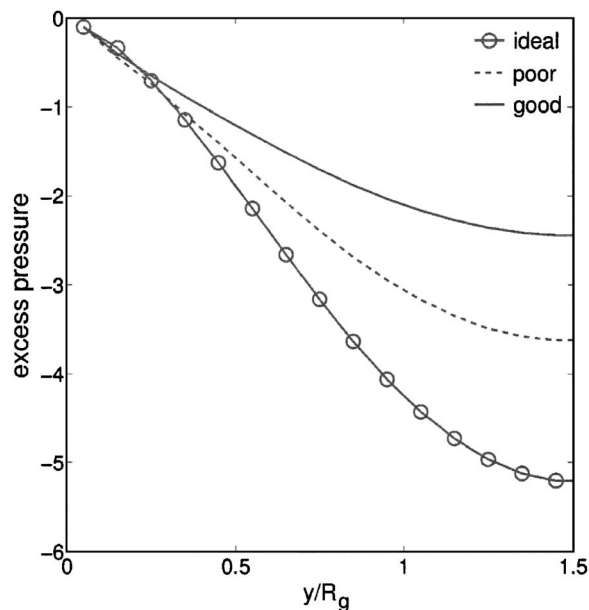
FIG. 4. Excess pressure across the channel for $N=100$ bead chain in solvents of different quality.

FENE chains in both poor and good solvents respectively. Each chain consists of $N=100$ beads and is placed in a channel of gap $H=3R_g$. The simulation parameters are summarized in Table III. The different spring model for the ideal chain is required due to the absence of DPD repulsive interactions, which for a FENE spring would yield zero equilibrium distance between connected beads because it exerts only attractive force. However, Fraenkel spring exhibits a nonzero equilibrium length explicitly. Furthermore, the results shown in Fig. 2 exhibited no dependence on the spring model. The above parameters are chosen to match the solvent quality as in Ref. 26. The exponent p [Eq. (7)] is set to 1.0, so that kinematic viscosity of the fluid is 0.2854.

Figure 3 shows the center-of-mass distribution (left) and the polymer bead distribution (right) for the ideal (Fraenkel) polymer and FENE chains in poor and good solvents. In contrast to the insensitivity of the distributions to different polymer models (Fig. 2), solvent quality has an effect on the polymer distribution. The ideal chain exhibits larger wall depletion (more confined distribution around the center)

compared to chains in good and poor solvents. A good solvent yields the smallest wall depletion and poor solvent curve falls in-between good solvent and ideal chain. The wall depletion force on a chain is expected to be repulsive due to the cost in free energy for the loss of the available polymer configurations near the wall. Furthermore, the depletion potential and resulting wall force are weaker for chains with excluded volume (EV) interactions (good solvent) than for ideal chains as theoretically predicted by Schlesener et al.,[28] where they concluded that EV interactions effectively reduce the depletion effect. As a result we observe larger wall depletion for ideal chains. This is illustrated by the pressure distribution across the slit. Figure 4 shows the excess pressure distribution in the channel with the solvent virial contribution and without the interbead-spring forces. Hence, only wall-polymer and solvent-polymer interactions contribute to the wall depletion. The excess pressure is obtained by subtraction of the equilibrium pressure in a large box. The pressure gradient for the ideal chain as we approach the wall from the centerline is larger than that of poor and good solvent. The larger pressure difference drives the polymer further away from the wall and contributes to larger wall depletion. The least pressure gradient and thus the smallest wall depletion was found for the good solvent case.

For complete analysis of the results we compute average polymer lengths in all three directions (x, y, and z) across the channel which characterize relative polymer shapes in the slit. We define local radius of gyration depending on the distance from the wall y as

$$R_g(y) = [(R_g^x(y))^2 + (R_g^y(y))^2 + (R_g^z(y))^2]^{1/2}, \qquad (12)$$

where $R_g^x(y) = \langle (1/N)\Sigma_{i=1}^N (x_i - x_{cm}(y))^2 \rangle$, $\langle \cdot \rangle$ denotes time averaging, x_i are bead coordinates in the x-direction, and $x_{cm}(y)$ is the center of mass at y. $R_g^y(y)$ and $R_g^z(y)$ are defined analogously. Figure 5 presents the local radius of gyration normalized by the unconfined R_g (left) and the ratio of $R_g^x(y)$ and $R_g^y(y)$ (right) which identifies the relative polymer shape across the channel. The left-hand plot in Fig. 5 shows that when confined in a slit the polymer occupies a volume slightly smaller than it would in the unconfined state, and that the chain takes on a more compact volume as it approaches the wall. The right-hand plot of Fig. 5 shows that
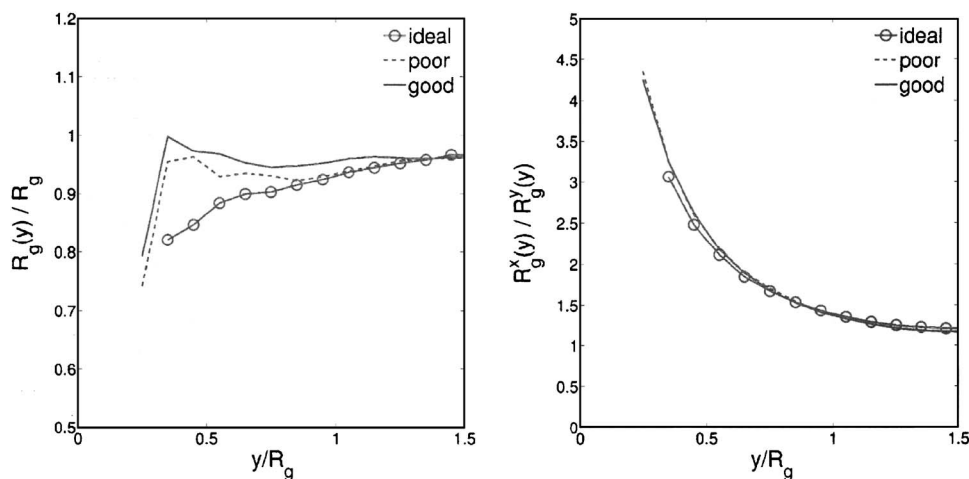

FIG. 5. Local radius of gyration (left) and relative shape of the polymer (right) for $N=100$ bead chain in solvents of different quality.

TABLE IV. DPD parameter sets used in wall-polymer-solvent interaction calculations.

spring	wall	k	r_{max}	a_{ss}	a_{pp}	a_{ps}	a_{wp}	R_g
FENE	neutral	10	2	25	25	17.5	17.5	2.1903
FENE	repulsive	10	2	25	25	17.5	25	2.1903

TABLE V. Simulation parameters for the channels of various gaps.

spring	k	r_{eq}	a_{ss}	a_{pp}	a_{ps}	a_{wp}	R_g
Fraenkel	10	0.7	25	25	17.5	17.5	1.9207

during the approach to the wall the chain elongates in the x and z directions relative to the y direction, and that its shape is nearly independent of solvent quality. As expected by symmetry $R_g^z(y)$ was found to be statistically identical to $R_g^x(y)$.

D. Wall-polymer-solvent interactions

In the simulations presented above wall-polymer and solvent-polymer interactions were identical. These are neutral walls for which no explicit adsorption or repulsion is expected. However, real walls are known to induce adsorption or repulsion (electrostatic) of polymers. A manipulation of relative wall-polymer-solvent interactions enables us to explicitly introduce net-attractive or repulsive wall forces on the polymer. This might correspond to adsorption and repulsion, respectively, but it requires further investigation. To this end, a polymer of $N=25$ beads in a good solvent was placed in a slit of gap $H=3R_g$. The simulation parameters are summarized in Table IV. Figure 6 presents the center-of-mass (left) and the bead (right) distributions for both neutral and repulsive walls. These results are compared to the center-of-mass distribution obtained by Ladd *et al.* in Ref. 8 using the LBM method for an $N=16$ bead chain in a channel also of gap $H=3R_g$. The repulsive wall exhibits larger depletion compared to neutral wall. Since the results of Ladd *et al.* fall between the neutral and the repulsive curves they correspond to a slightly repulsive wall. To verify that the boundary condition model (EBC-S) does not introduce extraneous effects, we have run analogous simulations using periodic BCs. Here, the computational domain is doubled in y direction to give a gap of $2H=6R_g$. The left half contains polymer solution confined between two parallel reflective walls at $y=0$ and $y=H$, and the right half is filled with the solvent. The system is set to be periodic in the y direction. Such a setup

corresponds to a perfectly neutral wall with no extraneous effects. The results were found to differ by no more than the statistical error.

E. Influence of the channel width

To this point we have presented results for channels of fixed gap $H=3R_g$. In this section the effect of channel width on the wall depletion layer is investigated with simulations of a $N=16$ bead chain confined in slits having gaps of $H=3R_g$, $4R_g$, $5R_g$, and $8R_g$, and with the parameters shown in Table V. Figure 7 presents the center-of-mass distribution of the simulated polymer confined in channels with gaps listed above. It also includes center-of-mass distributions normalized by their maximum magnitude c_{max} (correspondence is shown by arrows). For all channel widths the normalized distributions collapse onto a single curve which clearly demonstrates that the wall-polymer depletion region reaches no further than about $2.5R_g$. Consistency of this conclusion is tested by plotting the local radius of gyration normalized by the unconfined R_g and the ratio of components $R_g^x(y)$ and $R_g^y(y)$. Figure 8 shows that beyond a distance of about $2.5R_g$ both the local size (left) and the shape (right) of the polymer are unaffected by the wall.

F. The bead number *N* effect

Many theoretical results in polymer physics are asymptotic in the limit of large bead number N. Examples are the scaling laws for the radius of gyration and for the diffusion coefficient. To test the level of chain representation on the depletion layer we performed simulations for a set of chains having bead numbers $N=16$, 25, 100, and 500 in a channel of gap $H=3R_g$, and with the parameters shown in Table VI.
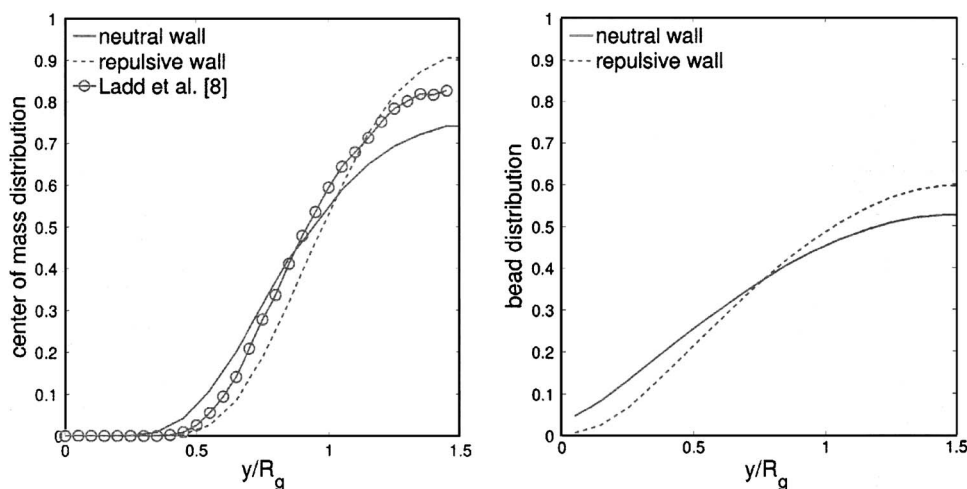

FIG. 6. Effect of wall-polymer-solvent interactions on the center-of-mass (left) and bead (right) distributions for a $N=25$ bead chain.
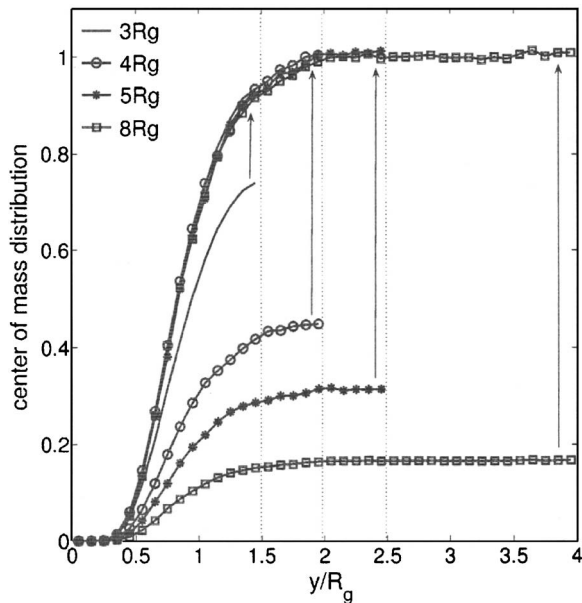
FIG. 7. Influence of gap size on the center-of-mass distribution for a chain of $N=16$ beads.

TABLE VI. DPD parameters used in bead number effect simulations.

spring	k	r_{max}	a_{ss}	a_{pp}	a_{ps}	a_{wp}
FENE	10	2	25	25	25	25

stricted to be a half-space, the longer chains suffer a larger loss in free energy and are subject to larger steric depletion forces. However, the analytical solution of Ref. 12 for ideal chains assumes the center-of-mass distribution will converge to an asymptotic curve as N becomes very large. In Fig. 10 the center-of-mass distributions, normalized by their maximum values c_{max}, for different bead numbers are compared with the asymptotic analytical solution. In the left-hand plot the distance from the wall is normalized by the equilibrium value of the radius of gyration R_g, and in the right-hand plot by the depletion layer thickness δ. The LBM results[8] are for an $N=16$ bead polymer in a channel of width $H=5R_g$. The curves in the figure show that, with lateral shifting, the numerical models closely capture the functional forms of the analytic solution, and that the depletion layer thickness provides the means for shifting the numerical distributions onto the analytic solution to produce an almost common curve. The agreement is remarkable since the numerical model features solvent explicitly represented by DPD particles whereas in the lattice model the solvent is implicit. Figure 10 (left) shows that, as expected, the shorter chains have distributions closer to the wall, and that, as N goes from 100 to 500, the discrepancy between the numerical and the analytic distribution becomes vanishingly small. For the latter the small discrepancy may be due to the solution having been carried out with a poor solvent condition, which as previously noted slightly weakens the depletion. The LBM curve has the largest discrepancy probably due to the relative wall-polymer-solvent interactions mentioned in Sec. III D and its small bead number N. In addition, our results agree well with the depletion layers calculated from Monte Carlo simulations by Berkenbos et al.[7] for tubes. They also investigated the limit of very small tubes, where the confinement greatly restricts the chain configurations. These distributions no longer resemble those in Figs. 7 and 10.
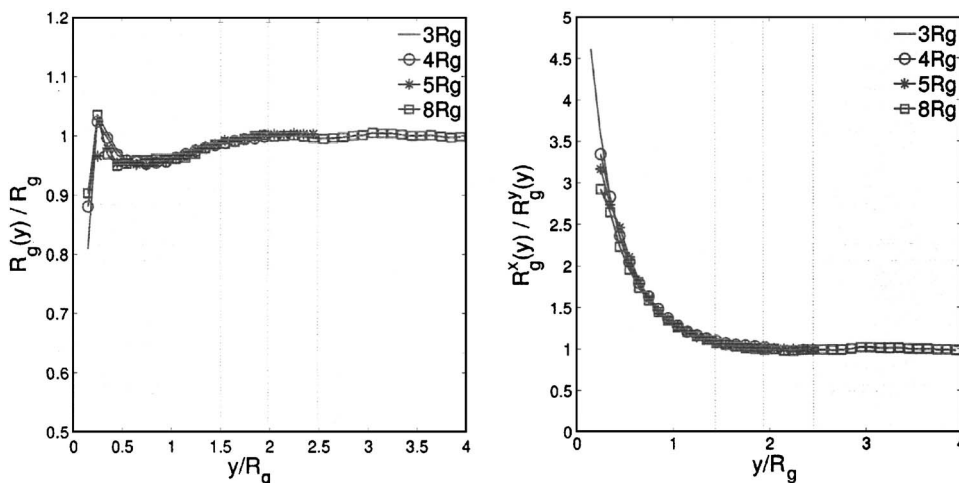
For the same simulations, Fig. 11 presents the local

Figure 9 shows the calculated center-of-mass distributions for this set of chains, and also the LBM results for N $=16$ in a channel of the same gap by Ladd et al.[8]

The gap dimensions for the simulations discussed above assumed the appropriate characteristic length to be the unconfined R_g. An alternative length scale, independent of molecular concepts, is derivable from concentration distributions such as those of Fig. 9. This depletion layer thickness δ is defined as,

$$\frac{\delta}{R_g} = \int_0^\infty \left(1 - \frac{c(z)}{c_{max}}\right)dz,$$ (13)

where $z=y/R_g$, $c(z)$ is the center-of-mass distribution, and $c_{max}=\max_{z\geqslant 0}[c(z)]$. From the distributions of Fig. 6, Eq. (13) yields $\delta/R_g=0.837$ for the neutral wall, $\delta/R_g=0.954$ for the repulsive wall, and for Ladd et al. $\delta/R_g=0.868$.

Longer chains are subject to a stronger depletion effect measured as a larger depletion layer thickness. Thus, it appears that, when the allowable configuration space is re-

FIG. 8. Local radius of gyration (left) and relative shape (right) for a chain of $N=16$ beads for various gaps.
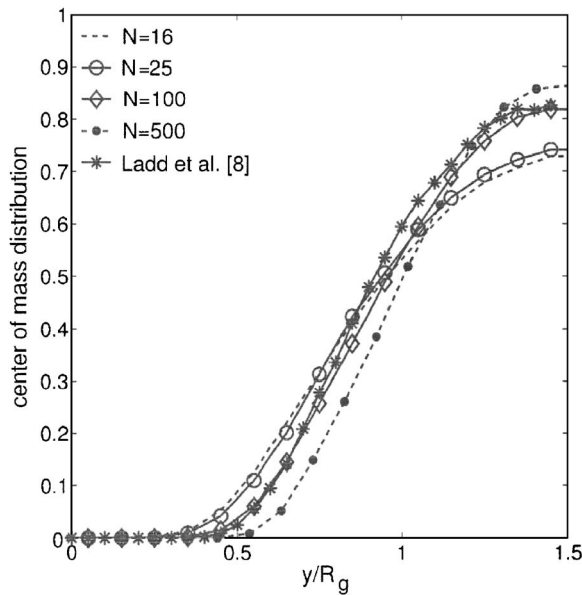
FIG. 9. Effect of bead number N on the center-of-mass distribution in a slit of $H=3R_g$.

$R_g(y)$ normalized by its unconfined value (left) and the ratio of $R_g^x(y)$ and $R_g^y(y)$ (right). The fact that the longest chains have the smallest normalized local $R_g(y)$ suggests that in the slit they adopt a more close-packed form than their smaller counterparts even though their relative shapes are about the same.

IV. POISEUILLE FLOW OF DILUTE POLYMER SOLUTIONS

This section results are presented for the Poiseuille flow of dilute polymer solutions confined between parallel plates separated by gap H. The Poiseuille flow is driven by a uniform pressure gradient as a force applied equally to both polymer and solvent DPD particles. Following[8] dynamic effects of the flow will be interpreted primarily with the Peclet number (Pe) defined as

$$Pe = \dot{\gamma}\frac{R_g^2}{D} = 4Sc\ Re\ \frac{R_g^2}{H^2}, \tag{14}$$

where $\dot{\gamma}=2V_c/H$ is the mean shear rate, V_c is the centerline velocity, and D is the polymer center-of-mass diffusion coefficient measured in equilibrium. The Schmidt number (Sc) and the channel Reynolds number (Re) are defined, respectively, by

$$Sc = \frac{\nu}{D}, \quad Re = \frac{V_c H}{2\nu} = \frac{\dot{\gamma}H^2}{4\nu}. \tag{15}$$

The discussion below invokes other Reynolds numbers based on the radius of gyration (Re_g) and Stokes–Einstein radius r_b (Ref. 24) of a polymer bead (Re_b) which can be defined, respectively, as

$$Re_g = \frac{\dot{\gamma}R_g^2}{\nu}, \quad Re_b = \frac{\dot{\gamma}r_b^2}{\nu}. \tag{16}$$

In some works,[9,10] Poiseuille flow results are interpreted in terms of the Weissenberg number $Wi=\tau\dot{\gamma}$, where τ is derived from the long-time relaxation of the stretched polymer chain in a stagnant solvent. Since both D and τ are derived from equilibrium data, they differ by at most a constant for a given chain. Furthermore, Wi can be expressed as a product similar to Eq. (14) with Sc replaced by $\tau\nu/R_g^2$, which is also a purely material property.

A. Velocity profiles

The Poiseuille velocity profile between walls placed at $y=0$, H for a non-Newtonian fluid with a power-law shear viscosity is given by

$$V(y) = V_c\left[1 - \left(\frac{y-H/2}{H/2}\right)^{1+1/n}\right],$$

$$V_c = \frac{n}{1+n}\left(\frac{\rho g}{\kappa}\right)^{1/n}\left(\frac{H}{2}\right)^{1+1/n}, \tag{17}$$

where n is the power-law index, g the uniform driving force per unit mass, κ the power-law shear-stress coefficient, and ρ the mass density.
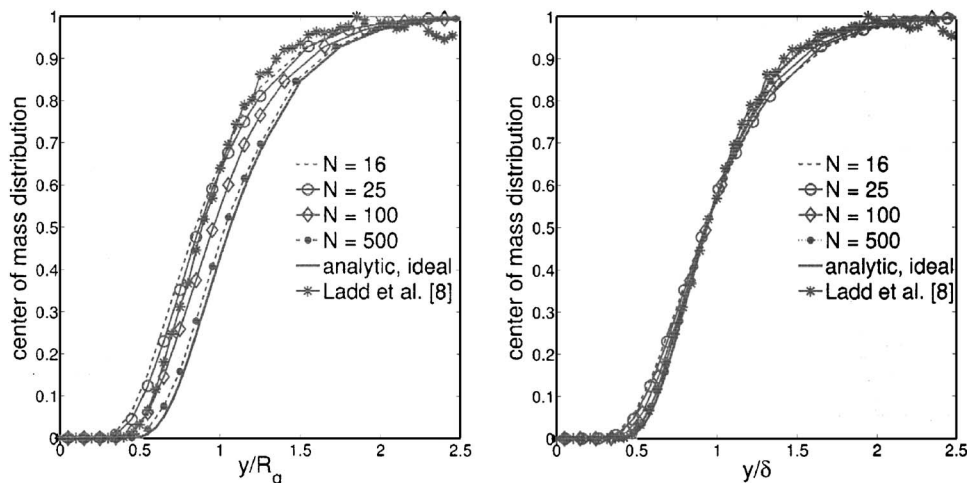

FIG. 10. Normalized center-of-mass distributions for different bead numbers compared with the analytical solution. The wall distance y is normalized by the unconfined R_g (left) and depletion layer thickness δ (right).
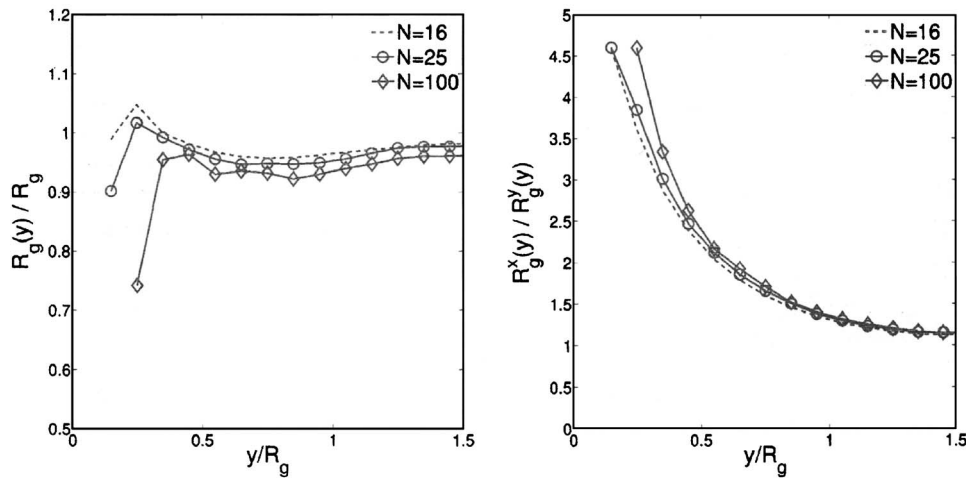
FIG. 11. Local radius of gyration (left) and relative shape (right) of the polymer for various N.

Figure [12] shows velocity profiles for an $N=100$ bead-chain solution in a gap of $3R_g$ at Pe=50, 100, and 200. The calculated velocity profiles of the suspension are well described by the power law [Eq. [(17)]] with $n=0.88$. The dashed curves are the corresponding Newtonian profiles for $n=1$. The average velocity of the particles within a slice Δy of the gap is assigned to be the local continuum velocity at the slice center. Hence, continuum wall velocities cannot be calculated directly. However, as expected from the particle boundary conditions of Sec. II C, there appears to be no slip at the wall since nearby velocities extrapolate to zero within statistical error. The Re, Re_g, and Re_b numbers scale linearly with Pe, and for the flow of Pe=200 they are Re=39.49, Re_g=17.55, and Re_b=0.055, respectively, where R_g=3.9235, r_b=0.22, and ν=0.2854.

B. Polymer migration

In addition to the hydrostatic depletion already presented, Poiseuille flow gives rise to further cross-flow migration of the polymer. This dynamic migration was investi-

FIG. 12. Poiseuille velocity profiles for several Pe's, $N=100$.

gated with a chain of $N=16$ beads with the parameters shown in Table [VII]. The solvent viscosity for all cases is $\nu=0.54$.

The simulations were performed at Pe numbers of 50, 100, and 200 for several channels. Figures [13]–[15] correspond to the gap widths $H=3R_g$, $5R_g$, and $8R_g$, respectively, and display the effect of the Pe and the Re numbers on the results for (i) the center-of-mass distributions, and (ii) chain conformation distributions imaged by computation of the three components of the local radius of gyration $R_g^x(y)$, $R_g^y(y)$, $R_g^z(y)$ normalized by their equilibrium components $R_g/\sqrt{3}$. In the figures the mean of the distribution is displayed as a horizontal line.

The center-of-mass distributions of Figs. [13]–[15], respectively, show the dynamic depletion layer to be steadily reduced relative to the hydrostatic case as Pe is increased, and that the effect is strongest for the smallest gap. In contrast, migration of polymer from the centerline towards the walls becomes more pronounced as the gap size increases, and between Pe=100 and 200 the significant development is a distribution with two off-center peaks, which is consistent with previous work,[8] and similar results obtained by various other methods were reported in Refs. [9]–[11] and [13]. Factors contributing to cross-stream migration are listed by Ladd et al.[13] as lift, rotation, stretching, and drift of the polymer from the wall. Graham et al.[10] attribute migration to two effects: chain-wall hydrodynamics and chain mobility gradients due to different conformations such as a stretched chain. The R_g distributions show the chain to be strongly stretched in flow direction x when subjected to high shear rates. In view of the hydrostatic preference for the centerline region, it seems counterintuitive that a chain prefers to occupy the region of higher shear rates away from the centerline with its vanishing shear rate. It is plausible to attribute the forces which drive the chain away from the center to be similar to those that control the effect of Segre–Silberberg in which[20,21]
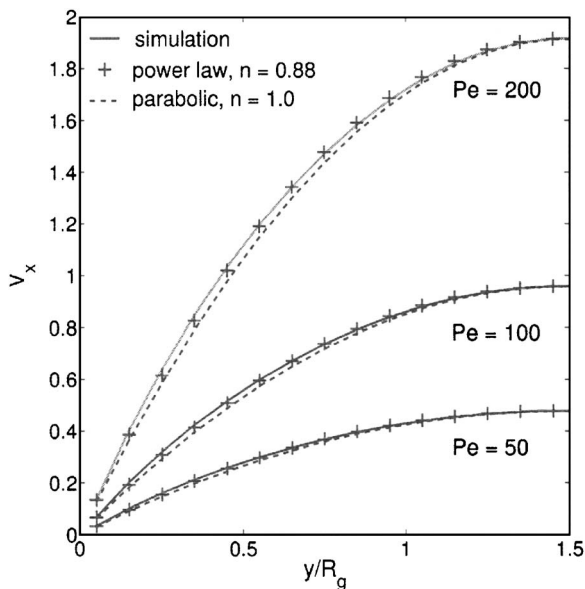
TABLE VII. Simulation parameters used in polymer migration calculations.

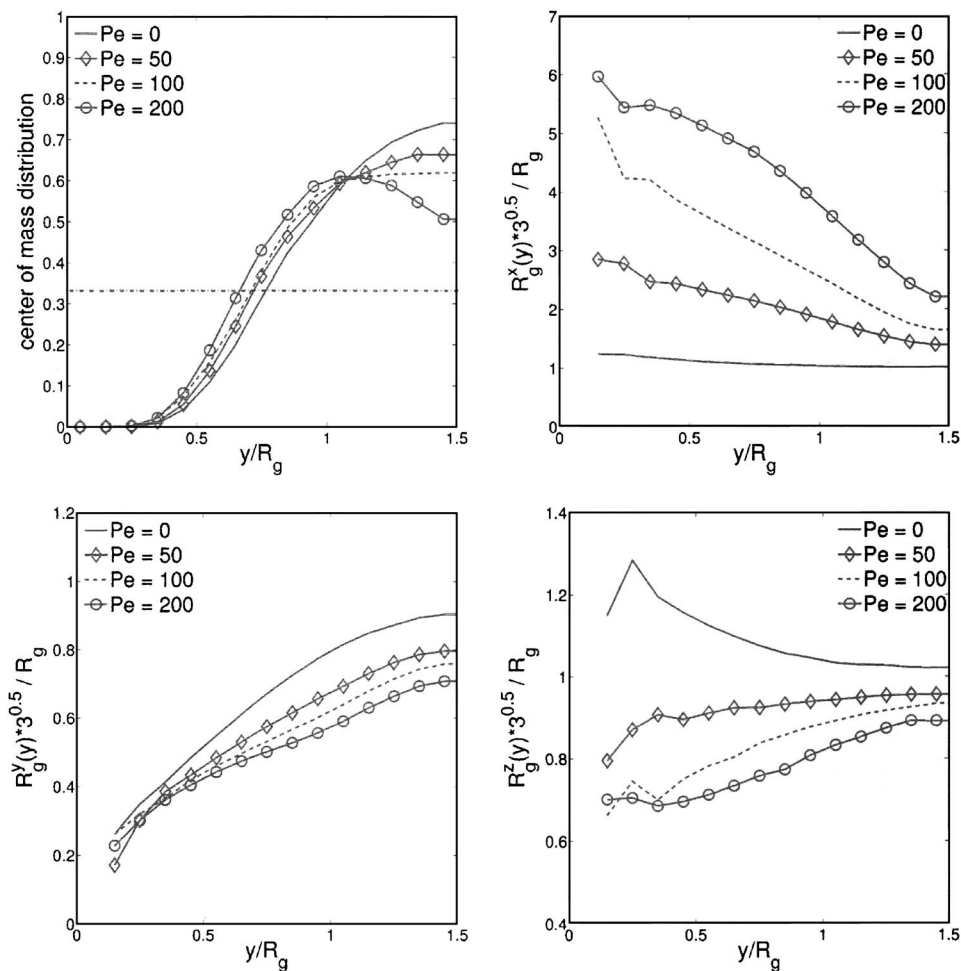| spring	k	r_{max}	a_{ss}	a_{pp}	a_{ps}	a_{wp}	R_g
FENE	10	2	25	25	25	25	1.36205

FIG. 13. Polymer center-of-mass (upper left) and conformation distributions of R_g^x (upper right), R_g^y (lower left), and R_g^z (lower right) in Poiseuille flow, $N=16$, $H=3R_g$.

a neutrally buoyant rigid sphere or ellipsoid[29] in a channel will migrate to an equilibrium position between wall and centerline due to the combined hydrodynamic effects of wall-particle interactions, velocity profile curvature and shear forces. The components of R_g show that, on average, the confined chain resembles an ellipsoid when viewed as an entity. However, flexibility and elasticity are not included explicitly in the Segre–Silberberg analysis although these factors are implicit in the definition (14) of the Peclet number. An alternative view is the chain as an ensemble of connected point-particles where each behaves as a sphere with a Stokes–Einstein radius,[24] and therefore is subject to the Segre–Silberberg forces. As reported in Refs. 30 and 31 the Segre–Silberberg effect for a suspension of particles strongly depends on the ratio of particle size to the channel width and Reynolds number of the flow based on the particle size. For the case of Pe=200, we have Re number in the range of 28.4–201.2 for the gaps $3R_g–8R_g$, and $Re_g=12.6$, $Re_b=0.33$, respectively. In our simulations the Re numbers are in the range of those given in Ref. 31 where results for Poiseuille flow predict particle migration to a stable position in-between the wall and the centerline. This appears to support our interpretation of the above results as the Segre–Silberberg effect. The results are qualitatively similar for the three channels. However, wall-molecule interactions appear to be a determining factor for the polymer distribution in small channels ($H \simeq 3R_g$). Wall-polymer repulsive forces are

dominant within a layer of about $2.5R_g$, and therefore in small slits the development of the off-center peaks in the distributions is observed only for relatively high Pe number when Segre–Silberberg forces are able to overwhelm wall steric repulsion. In contrast, for larger channels ($H \gtrsim 5R_g$) the off-center peaks in the polymer distributions appear at lower Pe, because wall-polymer forces act only within a near-wall layer and may not be present in the centerline region where shear forces have a migration effect. In addition, the distribution peaks coincide approximately with the maximum stretch (max. R_g^x, min. R_g^z) of the chain in the streamwise direction. The scatter in the distribution data clearly increases with channel size. This statistical defect for wider channels is a consequence of more expensive calculations for larger particle systems and longer times required for a chain to migrate a number of times across the slit.

The above argument suggests that polymer migration is characterized by at least three numbers: Pe, Re, and R_g/H. In the presence of inertia (Re>0) the Segre–Silberberg effect is to be expected, and this is in accord with the relatively high Re number cases presented above. Graham et al.[9] used the Brownian dynamics (BD) method to show ever increasing polymer migration towards the channel centerline with increasing Pe or Wi, where hydrodynamic inertia effects are excluded by use of only Stokes interactions for which the Segre–Silberberg effect vanishes. In particular, Stokes hydrodynamics accounts for very strong wall-polymer interactions.
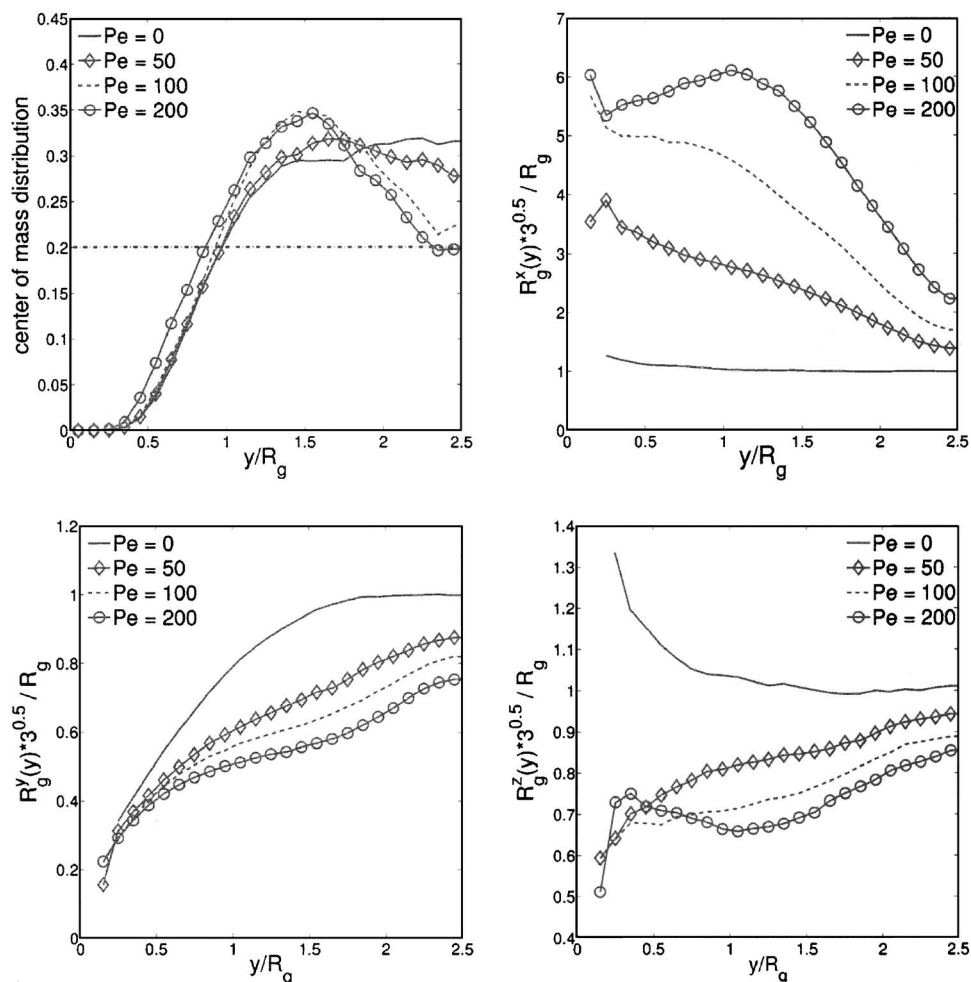
FIG. 14. Polymer center-of-mass (upper left) and conformation distributions of R_g^x (upper right), R_g^y (lower left), and R_g^z (lower right) in Poiseuille flow, $N=16$, $H=5R_g$.

However, as Wi increases, the channel Reynolds number must also increase. Analysis with linearized inertia [time dependent[32] (p. 354), Oseen[33]] suggests that as inertia increases from zero the typical leading Stokes interaction in the reciprocal distance is continuously replaced by the first-order inertial term typical of the unbounded case. This transition would appear to mark the inception of the Segre–Silberberg effect. The complexity of bead-spring suspensions does not permit "a priori" estimates of this Re range, but the Re values actually realized are germane to an assessment of the effect in Ref. 9. To this end, we have performed a number of DPD simulations with greatly reduced Re number. A 16-bead polymer solution having viscosity $\nu=14.019$ confined in the channel of $H=3R_g$ is subject to Poiseuille flow at Pe $=50$, 100, and 200. For Pe$=200$ we have Re$=0.041$, Re$_g$ $=0.018$, and Re$_b=4.66\times10^{-4}$, respectively. Figure 16 shows the center-of-mass distribution and chain conformations. The center-of-mass distributions of Fig. 16 differ only slightly from the hydrostatic case, in accord with the often-used description of low Re flow as "quasistatic." In contrast, the chain conformations resemble those at high Re shown in Fig. 13 for the same H/R_g rather than the hydrostatic conformations of Fig. 8. Unfortunately, the BD results of Graham et al.[9] do not include the hydrostatic case which would provide a critical comparison with the results of this paper. For Pe <100 polymer migration proceeds towards the channel centerline which suggests the dominance of wall-polymer inter-

actions. However, as Pe$\rightarrow200$, the center-of-mass distribution indicates a slight polymer migration away from the centerline which suggests that the Segre–Silberberg forces have become comparable with wall-polymer interactions. Moreover, evidence for the Segre–Silberberg effect at low Re number is provided by the perturbation theory of Ref. 30, the simulations of Ref. 31 and the experiments of Ref. 34. In conclusion, the results of this work indicate that polymer migration is governed by the Pe, Re, and R_g/H numbers which characterize wall-polymer interactions and the Segre–Silberberg effect. However, when Re$\rightarrow0$ [approximately $O(10^{-3})$] the Segre–Silberberg effect is negligible and polymer migration is then governed only by Pe and R_g/H, in accord with Refs. 9 and 10.

Other results, not included in this paper, indicate that polymer migration in Poiseuille flow is independent of the segment spring model (FENE and Fraenkel), and is governed almost entirely by the three numbers mentioned above which incorporate the characteristic polymer length and time scales [Eq. (14) and (15)]. However, we expect that increasing the number of beads in a chain will alter chain-wall interactions which this work has shown to affect migration. The hydrostatic results (Fig. 10) suggest that for large enough N the migration effect should be independent of the chain representation. However, even in the static case, 500-bead chains
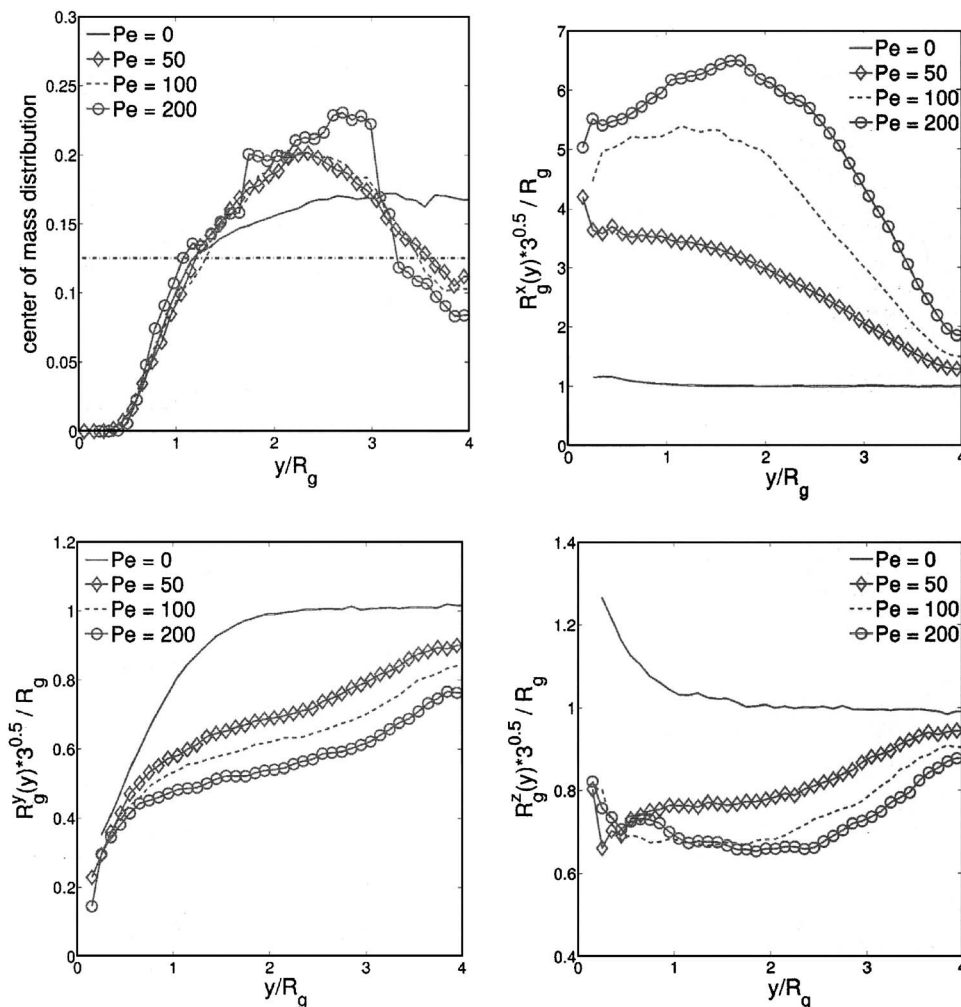
FIG. 15. Polymer center-of-mass (upper left) and conformation distributions of R_g^x (upper right), R_g^y (lower left), and R_g^z (lower right) in Poiseuille flow, $N=16$, $H=8R_g$.

were subject to the statistical difficulties mentioned above, and reliable results will be even more expensive to attain in the dynamic case.

The effect of solvent quality on migration is investigated with the 16-bead chain employed above in the channels with gaps of $H=3R_g$ and $4R_g$ for Pe=50 and 100. Figure 17 shows the center-of-mass distribution for solvents of different quality. Results predict stronger migration away from the centerline for good solvents than poor solvents. We attribute this to weaker wall depletion of polymers in good solvents as was pointed out in Sec. III C for the static case, and potentially stronger Segre–Silberberg effect due to the larger volume taken up by chains in good solvents compared to the more compact, less swollen, shape in poor solvents. As in the results of Figs. 13–16, the migration effect in smaller channels is attenuated by the stronger chain-wall interactions.

V. SUMMARY

For dilute polymer solutions in narrow channels we have investigated the hydrostatic depletion near walls for several bead-spring models, channel widths, number of beads, solvent quality, and wall-polymer-solvent interactions. The channel width was varied from 3 to 8 times R_g, the unconfined polymer radius of gyration. The center-of-mass and bead distributions and polymer shape measured by the components of the local radius of gyration were found to be

independent of the bead-spring model used in the simulations. Wall depletion and polymer shapes were found to be similar for channel gaps $H \gtrsim 3R_g$, and indeed distributions for all channel gaps collapse onto a single curve by normalization with the maximum concentration c_{max}, when other variables are fixed. The chain length specified with bead number N in the chain representation affects the depletion layer with short chains having narrower depletion layers than longer ones. However, as N becomes large ($N \gtrsim 500$) the depletion layer is independent of N, and the polymer distribution across the channel converges to the lattice theory solution for ideal chains near a purely repulsive wall. By scaling the distance from the wall with δ, an integral measure of depletion layer thickness [Eq. (13)], the center-of-mass distributions for all N can be collapsed onto the lattice theory asymptotic solution. Thus, with appropriate scaling, distributions for $N \sim O(10)$ adopt the shape of the very long, flexible chains of the lattice theory.

However, when a chain is immersed in a solvent of different quality its depletion layer properties change. A good solvent yields a thinner depletion layer than does a poor solvent, and by comparison the ideal chain has the strongest wall depletion. Finally, relative wall-polymer-solvent interactions or simply polymer boundary conditions also have a
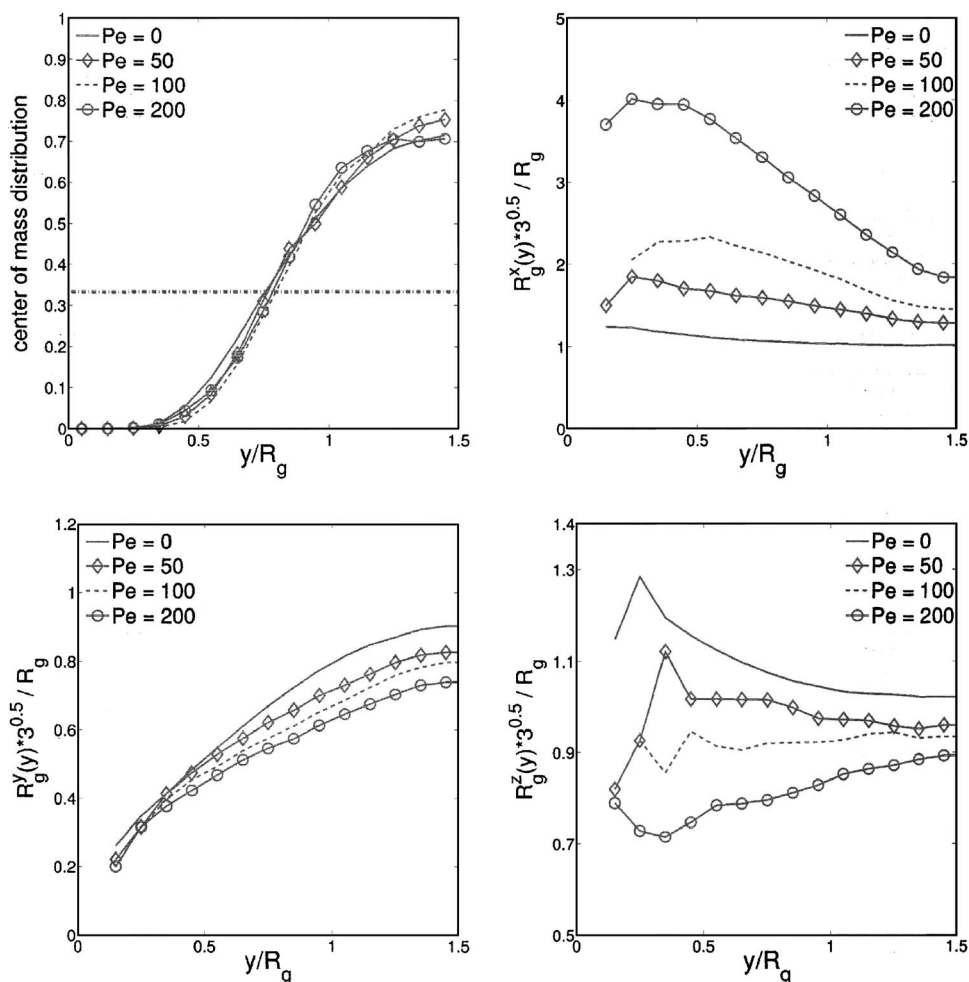
FIG. 16. Polymer center-of-mass (upper left) and conformation distributions of R_g^x (upper right), R_g^y (lower left), and R_g^z (lower right) in Poiseuille flow, $N=16$, $H=3R_g$. Low Re number.

strong effect on the depletion layer. Potentially, these interactions could be combined to control the depletion layer thickness and to model a wall adsorption.

In the dynamic case of Poiseuille flow we found that dilute polymer solutions exhibit slightly non-Newtonian behavior with velocity profiles corresponding to a power-law index of $n=0.88$ [Eq. (17)]. The hydrostatic depletion layer is affected by the flow, but beyond about a distance of $\delta \sim O(1)$ the center-of-mass distributions exhibit with increasing Pe and Re numbers ever stronger indications of migration toward an intermediate position between wall and centerline. At high enough Pe number Poiseuille flow induces in the distributions the new feature of two off-center peaks which correspond to the most probable channel positions. Simultaneously, the chains tend to stretch out in the direction of the shear planes. Thus, chains prefer an intermediate position between wall and centerline and not the middle of the channel where the shear rate vanishes. We attribute this to the hydrodynamic Segre–Silberberg effect which forces spheres and ellipsoids away from the centerline due to the
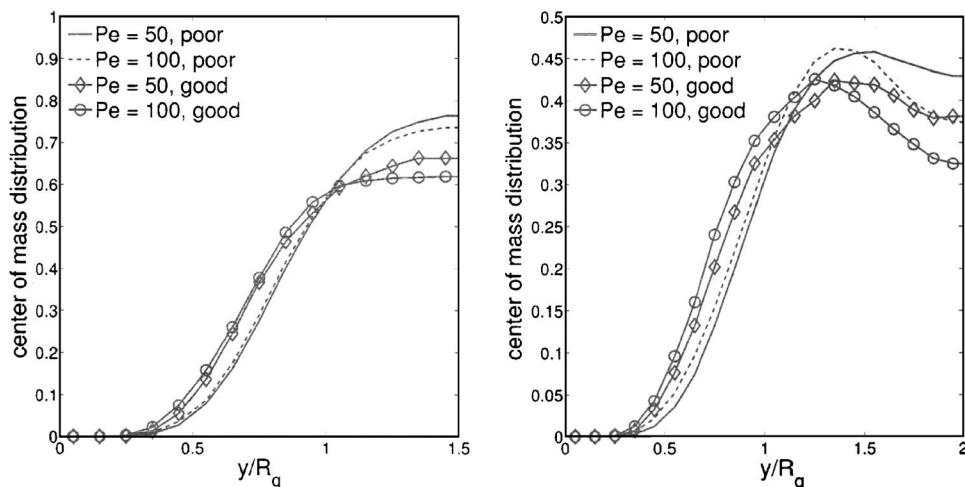

FIG. 17. Influence of solvent quality on center-of-mass distributions for Pe $=50,100$, $H=3R_g$ (left), and $H=4R_g$ (right).

shear gradient in Poiseuille flow. At high enough Re when hydrodynamic forces prevail over Brownian fluctuations, the quasistable polymer position in the channel appears to be determined by the balance of the wall-polymer hydrodynamic interactions and forces arising from Segre–Silberberg effect. In case of low enough Re number when the Segre–Silberberg effect becomes negligible polymer migration is governed by Pe number and proceeds mostly to the channel centerline due to wall-polymer interactions. We have shown that polymer migration is independent of the bead-spring model. However, the quality of the solvent, polymer boundary conditions, and the number of beads in the chain all affect polymer migration in the slit. We expect no dependence on number of monomers for large enough N. Finally, two off-center peaks in the distribution develop at lower Pe in the larger channels which is consistent with the known interaction length of several R_g for wall-polymer depletion. Hence the migration effect is more pronounced in the channels of larger widths.

ACKNOWLEDGMENTS

[1] P. G. de Gennes, *Scaling Concepts in Polymer Physics* (Cornell University Press, Ithaca, 1979).
[2] D. Aussere, H. Hervet, and F. Rondelez, Macromolecules **19**, 85 (1986).
[3] L. Fang, H. Hu, and R. G. Larson, J. Rheol. **49**, 127 (2005).
[4] Y. L. Chen, M. D. Graham, J. J. de Pablo, K. Jo, and D. C. Schwartz, Macromolecules **38**, 6680 (2005).
[5] A. Milchev and K. Binder, Eur. Phys. J. B **3**, 477 (1998).
[6] P. G. Bolhuis, A. A. Louis, J. P. Hansen, and E. J. Meijer, J. Chem. Phys. **114**, 4296 (2001).
[7] A. Berkenbos and C. P. Lowe, J. Chem. Phys. **127**, 164902 (2007).
[8] O. B. Usta, J. E. Butler, and A. J. C. Ladd, Phys. Fluids **18**, 031703 (2006).
[9] Y.-L. Chen, H. Ma, M. D. Graham, and J. J. de Pablo, Macromolecules **40**, 85 (2007).
[10] R. Khare, M. D. Graham, and J. J. de Pablo, Phys. Rev. Lett. **96**, 224505 (2006).
[11] J. A. Millan, W. Jiang, M. Laradji, and Y. Wang, J. Chem. Phys. **126**, 124905 (2007).
[12] E. Eisenriegler and R. Maassen, J. Chem. Phys. **116**, 449 (2002).
[13] O. B. Usta, J. E. Butler, and A. J. C. Ladd, Phys. Rev. Lett. **98**, 098301 (2007).
[14] H. Ma and M. D. Graham, Phys. Fluids **17**, 083103 (2005).
[15] P. J. Hoogerbrugge and J. M. V. A. Koelman, Europhys. Lett. **19**, 155 (1992).
[16] R. D. Groot and P. B. Warren, J. Chem. Phys. **107**, 4423 (1997).
[17] N. A. Spenley, Europhys. Lett. **49**, 534 (2000).
[18] R. D. Groot and K. L. Rabone, Biophys. J. **81**, 725 (2001).
[19] A. Maiti and S. McGrother, J. Chem. Phys. **120**, 1594 (2004).
[20] G. Segre and A. Silberberg, Nature (London) **189**, 209 (1961).
[21] G. Segre and A. Silberberg, J. Fluid Mech. **14**, 115 (1962).
[22] P. Espanol and P. Warren, Europhys. Lett. **30**, 191 (1995).
[23] X. Fan, N. Phan–Thien, S. Chen, X. Wu, and T. Y. Ng, Phys. Fluids **18**, 063102 (2006).
[24] V. Symeonidis, B. Caswell, and G. E. Karniadakis, J. Chem. Phys. **125**, 184902 (2006).
[25] D. A. Fedosov, I. V. Pivkin, and G. E. Karniadakis, J. Comput. Phys. **227**, 2540 (2008).
[26] Y. Kong, C. W. Manke, W. G. Madden, and A. G. Schlijper, J. Chem. Phys. **107**, 592 (1997).
[27] J. A. Backer, C. P. Lowe, H. C. J. Hoefsloot, and P. D. Iedema, J. Chem. Phys. **122**, 154503 (2005).
[28] F. Schlesener, A. Hanke, R. Klimpel, and S. Dietrich, Phys. Rev. E **63**, 041803 (2001).
[29] D. Qi, L. Luo, R. Aravamuthan, and W. Strieder, J. Stat. Phys. **107**, 101 (2002).
[30] P. Vasseur and R. G. Cox, J. Fluid Mech. **78**, 385 (1976).
[31] J. Feng, H. H. Hu, and D. D. Joseph, J. Fluid Mech. **277**, 271 (1994).
[32] J. Happel and H. Brenner, *Low Reynolds Number Hydrodynamics* (Prentice-Hall, Englewood Cliffs, NJ, 1965).
[33] H. Brenner, J. Fluid Mech. **11**, 604 (1961).
[34] D. H. Douglas–Hamilton, N. G. Smith, C. E. Kuster, J. P. W. Vermeiden, and G. C. Althouse, J. Androl **26**, 107 (2005).